Dimerization and dynamics of angiotensin-I converting enzyme revealed by cryoEM and MD simulations

Jordan M. Mancl[1], Xiaoyang Wu[1], Minglei Zhao[2], Wei-Jen Tang[1]

1. Ben-May Department for Cancer Research, The University of Chicago, Chicago, Illinois, United States

2. Department of Biochemistry and Molecular Biology, The University of Chicago, Illinois, United States

Keywords: Angiotensin-I converting enzyme, hypertension, amyloid peptide, cryoEM, all-atom MD simulations.

Author contributions: J.M.M. and W.-J.T., designed the project. X. W. transduced and selected ACE-expression HEK293F cells. J.M.M. and W.-J. T. performed the expression and purification of ACE. J.M.M. performed cryoEM grid preparation, data acquisition and processing assisted by M.Z. and overseen by W.-J. T., and M. Z. J.M.M. built and refined cryoEM structural models and performed heterogeneity analysis. J.M.M. and W.-J. T. performed all-atom MD simulations and analysis. J.M.M. and W.-J.T. wrote the manuscript and all authors contributed to manuscript finalization.

Acknowledgement: We are grateful to Mahira Aragon for grid preparation using Chameleon, Kasahun Neselu for data collection, and Marc Auréle Gilles for assistance with RECOVAR analysis. This work was supported by the NIH grant GM121964 to W.-J. Tang. Some of this work was performed at the National Center for CryoEM Access and Training (NCCAT) and the Simons Electron Microscopy Center located at the New York Structural Biology Center, supported by the NIH Common Fund Transformative High Resolution Cryo-Electron Microscopy program (U24 GM129539,) and by grants from the Simons Foundation (SF349247) and NY State Assembly.

Abstract

Angiotensin-I converting enzyme (ACE) regulates the levels of disparate bioactive peptides, notably converting angiotensin-I to angiotensin-II and degrading amyloid beta. ACE is a heavily glycosylated dimer, containing 4 analogous catalytic sites, and exists in membrane bound and soluble (sACE) forms. ACE inhibition is a frontline, FDA-approved, therapy for cardiovascular diseases yet is associated with significant side effects, including higher rates of lung cancer. To date, structural studies have been confined to individual domains or partially denatured cryoEM structures. Here we report the cryoEM structure of the full-length, glycosylated, sACE dimer. We resolved four structural states at 2.99 to 3.65 Å resolution which are primarily differentiated by varying degrees of solvent accessibility to the active sites and reveal the full dimerization interface. We also employed all-atom molecular dynamics (MD) simulations and heterogeneity analysis in cryoSPARC, cryoDRGN, and RECOVAR to elucidate the conformational dynamics of sACE and identify key regions mediating conformational change. We identify differences in the mechanisms governing the conformational dynamics of individual domains that have implications for the design of domain-specific sACE modulators.

42 **Introduction**

43 Angiotensin-I converting enzyme (ACE) is an M2 clan zinc metalloprotease
44 (EC3.4.15.1) located on the plasma membrane and in the extracellular milieu (1-3). ACE
45 plays a crucial role in the renin-angiotensin system by converting angiotensin I to the
46 potent vasoconstrictor angiotensin II, and in the kinin-kallikrein system by degrading
47 bradykinin, a potent vasodilator. Inhibiting ACE is a primary approach for treating
48 hypertension and is a proven therapy for heart failure, diabetic nephropathy, and other
49 cardiovascular and renal dysfunctions (4). However, ACE inhibition has known side
50 effects, e.g., dry cough and angioedema, and has been linked to higher rates of lung
51 cancer (Wu *et al*., 2023). This is partly because ACE also degrades a diverse range of
52 peptides, resulting in complex physiological outcomes due to the interplay in altering
53 levels of these peptides (4-8). Furthermore, ACE degrades amyloid β (Aβ), which is
54 associated with the progression of Alzheimer's diseases (9-12). Overexpression of ACE
55 in myelomonocytes substantially reduced Aβ load and prevented Alzheimer's disease-like
56 cognitive decline in mice (13). However, the brains of some Alzheimer's disease patients
57 showed upregulation of the renin-angiotensin system which led to deleterious effects and
58 ACE inhibition was beneficial (14-16). These studies indicate that global ACE inhibition
59 could be either beneficial or harmful for individual Alzheimer's patients, and underscores
60 a need for better understanding the molecular mechanisms governing ACE function and
61 substrate selectivity to develop more selective, improved, ACE inhibitors and expand
62 ACE-based therapies (14-16).

63 ACE is a 180 kDa heavily N-linked glycosylated type 1 transmembrane protein with
64 two homologous catalytic domains residing at the N- and C-terminal ends (ACE-N and
65 ACE-C) in its extracellular region (1, 3, 17). The ACE extracellular region can be released
66 via proteolytic cleavage near the transmembrane region by ADAM family protease(s),
67 generating soluble ACE (sACE) (18). ACE belongs to the cowrin (cowry like) family of zinc
68 metallocarboxypeptidases because its catalytic domain is ellipsoidal and contains a long,
69 deep, yet narrow catalytic cleft (19). ACE is known to cleave short peptides, such as
70 angiotensin I (decapeptide) and bradykinin (nonapeptide) by removing the C-terminal two
71 amino acid residues. Different from the funnelin family of metallocarboxypeptides that
72 contains a funnel-like cavity, the catalytic cleft of ACE can accommodate entire
73 oligopeptides and ACE has been shown to cleave multiple discrete sites on Aβ outside

74 the C-terminal end (11). Thus, it is more accurate to refer to ACE as an endopeptidase
75 with dipeptidyl carboxylase activity.

76 Extensive crystallographic studies of ACE-N or ACE-C alone and in complex with
77 various inhibitors and a catalytic product, angiotensin-II, have elucidated the overall
78 structures of ACE catalytic domains and molecular details of the catalytic pockets (2, 20-
79 23). The structures indicate that each domain is comprised of three sub-domains and
80 offer insight for the substrate preferences around cleavage sites and the promiscuity of
81 each domain toward short peptide substrates. Furthermore, they reveal the orientation of
82 substrate binding sites around scissile bond, indicating that the entire oligopeptide
83 substrates need to be engulfed into the catalytic chamber of ACE catalytic domain (20,
84 22, 23).

85 However, the catalytic pocket of ACE in the closed state is not large enough to
86 accommodate the entrance of all its known substrates, particularly Aβ, to permit the
87 observed cleavage pattern. Thus, similar to other Aβ-degrading proteases, such as insulin
88 degrading enzyme (IDE), presequence protease (PreP), and neprilysin (NEP), ACE must
89 undergo a large-scale open-closed transition to capture and degrade larger peptide
90 substrates such as Aβ (24-26). Recent open state structures of sACE-N, sACE monomer,
91 and a sACE-N dimer, along with molecular dynamics (MD) simulations of sACE-C, have
92 begun to reveal the conformational heterogeneity, though it remains under-studied (27-
93 29).

94 The extracellular domains of ACE are readily dimerized in the membrane-bound
95 and soluble forms. Both the ACE-N and ACE-C domains within the ACE monomer are
96 catalytically active and each has its own substrate preferences (5, 11, 30). For example,
97 ACE-N can convert Aβ1-42 to Aβ1-40, which is less amyloid fibril-prone than Aβ1-42 but
98 ACE-C cannot (11). Accumulating evidence support a complicated interplay between
99 ACE-N and ACE-C within the ACE dimer. Enzyme kinetics analysis suggests negative
100 cooperativity between two catalytic domains (31-33). However, ACE also exhibits positive
101 synergy toward Aβ cleavage and allostery to enhance the activity of its binding partner,
102 bradykinin receptor (11, 34). Recently, cryoEM structures of soluble dimeric apo-sACE
103 were reported (28); however, due to the poor resolution/denaturation of sACE-C, only full-
104 length sACE monomer or dimeric sACE-N was reported yet the conformations preclude

105 full-length sACE dimerization due to the severe steric crash between sACE-C domains.
106 Here, we present four discrete cryoEM structures of full-length sACE that contain all four
107 catalytic domains (Fig. 1A). This is followed by cryoEM heterogeneity analysis and all-
108 atom MD simulations. Together, our analyses provide structural insights into domain
109 interactions, open-closed transitions of the catalytic domain, and conformational
110 dynamics of soluble dimeric ACE.

111 **Results**

112 **Structures of the full-length sACE dimer determined by single particle cryoEM**

113 Soluble human ACE (sACE), which includes the entire extracellular region of ACE,
114 was expressed in HEK293F cells and purified from culture supernatant using an ion
115 exchanger (Source Q) followed by size exclusion chromatography (Superdex S200).
116 Buffer conditions suitable for single particle cryoEM analysis were identified and
117 optimized using differential scanning fluorometry (Figure S1). Purified sACE was then
118 vitrified using a Vitrobot, and a dataset of ~3,600 micrographs was collected on a 300
119 keV Titan Krios equipped with a Gatan K3 camera at the University of Chicago Advanced
120 Electron Microscopy Facility (Table S1). The data was processed in cryoSPARC v4.4.0
121 (Figure S2). After filtering ~1.1 million picked particles to ~378K using 2D and 3D
122 classification, three classes were identified (Figure 1, Figure S2). Of these, ~268K
123 particles mapped to a dominant 2-domain class reconstructed as an ACE-N dimer, while
124 ~21K particles mapped to a minor 3-domain class containing two ACE-N and only one
125 ACE-C, reminiscent of the recently published ACE cryoEM structure (28). The remaining
126 89K particles mapped to a full-length ACE dimer containing two ACE-N and two ACE-C,
127 which was refined to 3.65Å resolution (Figure 1C, S2, Movie S1, Table S1).

128 The partial denaturation of macromolecules during vitrification has been attributed
129 mainly to repeated exposure of the macromolecules to the air-water interface (35, 36).
130 The sACE-C domain was shown to be less stable than the ACE-N domain (37), so we
131 hypothesized that repeated exposure to the air-water interface could cause preferential
132 denaturation of ACE-C. We have previously showed that preferential denaturation of
133 human PreP occurred in one of its two homologous domains and that faster vitrification
134 using Chameleon significantly prevented such preferential denaturation (24). Therefore,
135 we collaborated with the National Center for CryoEM Access and Training (NCCAT) to

136 prepare sACE grids using Chameleon (38). Chameleon preparation reduced the time the
137 sample spends on the grid before freezing by more than 10-fold. We collected a new
138 dataset of ~18,000 micrographs and our 2D classification revealed a higher percentage
139 of particles for four-domain classes than those prepared using the Vitrobot (Figure 1B).
140 However, our 3D classification still showed the existence of structures of the ACE-N only
141 dimer and those containing two ACE-N and one ACE-C (Figure S3). This indicates that
142 the reduction in vitrification time using Chameleon reduced but did not prevent preferential
143 denaturation.

144 From these data, we obtained a map for a consensus ACE structure that achieved
145 a resolution of 2.8Å. However, while the core region showed excellent map quality, the
146 map quality for the dynamic regions corresponding to the open-close transition of ACE
147 catalytic domains was poor, suggesting multiple discrete conformational states exist. We
148 thus performed 3D classification and reconstructed three distinct conformational states of
149 full-length apo-ACE at resolutions of 2.99Å, 3.05Å, and 3.15Å (Figure 1C, S3, Movie S2-
150 4, Table S1). We refer to these ACE dimer structures by their resolutions, namely ACE-
151 2.99, ACE-3.05, and ACE-3.15, along with the structure from data obtained using the
152 Vitrobot, ACE-3.65. Given the rich structural information from more than 50 reported
153 crystal structures of ACE and one recently reported cryoEM study of ACE, below we focus
154 on the new insights that our ACE dimer structures offer (2, 20, 22, 28, 39, 40).

155 **The overall structures of sACE dimers and structural insight into dimerization**

156 Soluble ACE has two homologous catalytic domains: ACE-N (amino acids 31-644)
157 and ACE-C (amino acids 645-1231). Based on the comparison of various catalytic
158 domains of our ACE dimer structures, we subdivide each catalytic domain of ACE into
159 three subdomains: D1a, D1b, and D2 for ACE-N, and D3a, D3b, and D4 for ACE-C
160 (Figure 1A). These three subdomains in either ACE-N or ACE-C form a catalytic chamber.
161 The catalytic zinc ion is coordinated by the canonical HEXXH motif residing in the D1b
162 and D3b subdomains (Figure 1A). Four sACE dimer structures manifest as pseudo-
163 symmetric C2 homodimers across the dimer interface. The dominant symmetry-breaking
164 features are the degrees of displacement between D1 and D2 or between D3 and D4,
165 leading to changes in solvent accessibility to the catalytic pockets.

Based on the openness of the catalytic chamber, defined at the distance between the D1/3a and D2/4 helices that gate access, we classified sACE-N into three conformational states: open (O), intermediate open (I), and closed (C) (Figure 2A); sACE-C is significantly less open than sACE-N in our structures, and is only classified into intermediate (I) and closed (C) states (Figure 2B). The four sACE dimer structures differ mostly by the degrees of openness of their four catalytic domains (Figure 2C, D). Our sACE-2.99 and sACE-3.65 structures are globally similar, both contain sACE-N domains in the open and intermediate states and sACE-C domains in the closed and intermediate states. In sACE-3.05, both sACE-N domains adopt an open state, while the sACE-C domains adopt an intermediate and closed state. In the sACE-3.15 structure, one subunit has both sACE-N and sACE-C adopting a closed conformation, while the other subunit has an open sACE-N domain and an intermediate sACE-C domain.

Our four cryoEM structures of sACE provide the structural basis for sACE dimerization. sACE dimerization is mediated by interfaces between D2 subdomains and D4 subdomains of sACE monomers. The D2 and D4 subdomains generally have much lower B-factors than the D1 and D3 subdomains (Figure S4). The interaction of the D4-D4 subdomains is analogous to the D2-D2 interaction, yielding an RMSD of ~1 Å² when aligned (Figure 3A). The primary source of variation is a general rigid body shift away from the interaction interface for non-interacting regions in the D4-D4 region compared to the D2-D2 region. The observed D2-D2 interface is consistent with one of three possible contacts between sACE-N in the non-crystallographic symmetry mates from previous crystallographic analysis of sACE-N and the previously published cryoEM structure (Figure S5). In total, the interface between sACE monomers buries a surface area of approximately 1,900 Å². Although sACE-N and sACE-C are structurally analogous, their respective interfaces (sACE-N/N and sACE-C/C) are not equivalent. The sACE-N/N interface is larger and stronger, burying a surface area of approximately 1,150 Å², compared to a buried surface area of approximately 750 Å² for the sACE-C/C interface.

The interface between sACE-N is formed by a hydrophobic core, anchored by a Y494 π-stacking interaction, and flanked by salt bridges formed by R482 and R487 as well as E241 and E248 along with a collection of polar and van der Waal contacts (Figure 3B). The dimer interface between two sACE-N domains is completed by glycan-glycan interactions between the glycans attached to N111, which is consistent with the role of

198 glycosylation in sACE dimerization (Figure 3C) (41). However, the central residues that
199 form the hydrophobic core of the interface between sACE-N are not present in the
200 interface between sACE-C. Instead, the sACE-C interface is formed by a symmetric salt
201 bridge between K1096 and E1089, side chain-backbone interactions, and van der Waals
202 contacts (Figure 3D).

203 **Conformational states of sACE catalytic domains**

204 The comparison of our dimeric sACE cryoEM structures of reveals the
205 conformational dynamics of sACE catalytic domains. The four sACE dimer structures
206 represent different combinations of open, intermediate, and closed states of ACE catalytic
207 domains (Figure 2). By aligning each sACE-N and sACE-C region in our structures to the
208 D2/4 domain, it becomes clear that our structures represent a continuous gradient of
209 structural heterogeneity, ranging from the most closed state to the most open state (Figure
210 S6).

211 The comparison of sACE-N in its open and closed states reveals the structural
212 basis for the open-to-closed transition of this domain. Our structures show that when the
213 tip connecting the two long helices of the D1a subdomain moves away from the D2
214 subdomain, resulting in the open state, the opposite end of the helix moves closer to the
215 D2 subdomain, as if the helix were balanced upon a fulcrum (Figure 4A, B). Detailed
216 structural analysis indicates that the fulcrum is primarily formed by the salt bridge between
217 two highly conserved residues: E95 in the D1a subdomain and R137 in the D2
218 subdomain. To stabilize the open state, additional salt bridges are formed, with D218 in
219 the D2 subdomain pairing with K102 in all cases and occasionally with R125 in the D1a
220 subdomain (Figure 4A). The loss of this salt bridge in the closed state is compensated for
221 by the formation of a network of van der Waals interactions between the D1a and D2
222 subdomains that stabilize the closed state. The transition between open and closed states
223 is likely influenced by the binding of substrates and reaction products during the ACE
224 catalytic cycle. Although a similar fulcrum mechanism is not evident in the sACE-C
225 domain, the connection between the D3a and D2 subdomains would act as a lever to
226 pivot sACE-C from the closed to the open state. The closed state of sACE-C is also
227 stabilized by a network of van der Waals contacts between the D3a and D4 subdomains.

228 On average, sACE-N is more open than sACE-C, likely due to multiple factors
229 (Figure 2D). In sACE-N, the D1a subdomain is at the N-terminal end of sACE, allowing
230 for a greater range of motion (Figure 4B), while the fulcrum and stabilization mechanisms
231 can maintain sACE-N in a more widely open state (Figure 4A). Conversely, in sACE-C,
232 the motion of the D3a subdomain is constrained by its connection to the D2 subdomain
233 (Figure 4C). Additionally, there are sequence differences at the interface between the
234 three subdomains of sACE-N and sACE-C. In the most closed state—the B chain sACE-
235 C domain of the sACE-3.05 structure—residues from all three subdomains, including
236 I678, V753, V955, and V956, form a hydrophobic latch that stabilizes the closed state
237 (Figure 4D). The hydrophobic latch in sACE-N is weaker because the residue
238 corresponding to V753 has been replaced with a threonine (Figure 4D).

239 We performed a series of all-atom molecular dynamics (MD) simulations to explore
240 the conformational dynamics of sACE. A total of 8 apo-sACE simulations were conducted,
241 comprising four simulations with non-glycosylated sACE (>1.8 μs each) and four with
242 sACE where all 12 N-linked glycosylation sites have complex glycans (>2 μs each) (Movie
243 S5, S6). Glycan orientations were randomized prior to each simulation to avoid bias. We
244 did not observe a substantial difference in the global conformational dynamics between
245 our sets of simulations with and without glycans. The domain motions of these simulations
246 are summarized in Table S2. Below, we focus on the general features from these
247 simulations.

248 RMSD analysis reveals that the dominant source of conformational change in our
249 simulations is the open-close transition between the D1/3 and D2/4 domains (Figure S7).
250 The D2/D2 and D4/D4 regions are the most stable, with the bulk of conformational
251 changes localized to the D1/D3 domain. Within the D1/3 domain, we observed that the
252 D1/3a motion was not always correlated with D1/3b or D2/D4, meaning that at a given
253 time, D1/3a could move along with D1/3b, or with D2/D4, or independently. Consistent
254 with our structural analysis, our MD simulations also indicate that sACE-N displays a
255 much wider range of opening geometries than sACE-C. Most of our MD simulations
256 rapidly closed, preventing an effective comparison of the open vs closed state dynamics.
257 However, the slowest closing simulation did reveal a correlation with our previously
258 described “fulcrum” mechanism of opening for sACE-N (Figure 4A). Our simulation
259 revealed that the K102-D215 interaction was maintained for the entire time that sACE-N

adopted an open conformation, yet this interaction was lost when sACE-N transitioned to the closed state (Figure 4E).

The MD simulation of glycosylated ACE provides additional structural insights into the structure and functions of N-linked glycosylation of ACE. Glycosylation is shown to affect the folding, secretion, and stability of ACE (42, 43). Our MD simulation reveals that the dynamics of 12 N-linked glycans cover a large surface area of ACE, shielding it from environmental insults (Figure S8). Consistent with observations from our Coulomb potential density maps and previously published data, we observed a substantial and persistent inter-subunit interaction between glycans from N111 (Figure 3C). From room mean square fluctuation (RMSF) analysis, glycosylation was found to increase the overall dynamicism of sACE (Figure S9). Furthermore, while there are N-linked glycans near the catalytic chamber, particularly those at the tip of D1a and D3a, they were highly dynamic and did not occlude access to the catalytic chamber. This is consistent with the observation that deglycosylation only modestly increases the enzymatic activity of ACE (44-46).

We also performed three simulations on the non-glycosylated sACE monomer (>1 microsecond each) (Table S2). We observed the expected intra-subdomain open-closed motions in sACE-N and sACE-C that were also observed in the simulations of ACE dimer. We also observed that the motion of sACE-C relative to sACE-N was significantly greater in our monomer simulations compared to our dimer simulations. This suggests that dimerization places significant constraints upon the conformational dynamics of sACE. Previous work has defined the conformational dynamics of sACE from cryoEM data where both sACE-C domains were not resolved. Given our observations from the monomeric and dimeric MD simulations, we endeavored to understand the conformational heterogeneity present within our cryoEM data to better understand the impact of dimerization on sACE dynamics.

CryoEM heterogeneity analysis of sACE

CryoEM structures are ensemble averages of many aligned particle images. Recently, there have been many approaches developed to understand the particle heterogeneity present within a cryoEM structure as a proxy for molecular motion (47). We employed three methods of heterogeneity analysis: cryoDRGN, RECOVAR, and 3D

Variability Analysis (3DVA) (48-50). CryoDRGN employs neural networks to resolve structural heterogeneity in a nonlinear, multidimensional latent space, while RECOVAR and 3DVA both employ linear subspace methods. 3DVA finds the linear subspace by an alternating optimization scheme to capture image variations while RECOVAR utilizes a regularized covariance estimator to identify subspaces that best capture the distribution of states.

We conducted this analysis on both of our datasets and found the results to agree, therefore, we focus on the larger, and higher-resolution dataset collected at NCCAT below. For analysis, the entire particle set, prior to 3D classification and consisting of ~170k particles, was utilized. The particle alignments from the same C1 consensus refinement were used as input for each of the three methods as current methods to investigate particle heterogeneity are highly dependent upon initial pose assignment of individual particles. Globally, all three methods agreed with our ensemble structures, in that the dominant source of structural variability within our particle population could be described by the open-closed transition of individual domains, and that sACE-N displayed more variability than sACE-C.

Initially, we performed 3D variability analysis (3DVA) in cryoSPARC to provide a direct comparison to the previously published analysis of the partial ACE cryoEM structure (51) (Figure 5A). Trajectories were reconstructed along the top 5 principal components of variance (Movie S7). Surprisingly, the trajectory describing the variance along the first principal component vector suggests a dominant inter-domain motion, where the sACE-N/N region bends towards the sACE-C/C region. The trajectories along the remaining principal component vectors comprise varying combinations of individual domains undergoing the open-close transition. Consistent with our previous observations, the range of presumptive motion in these trajectories is greater in sACE-N than sACE-C. Previous 3DVA performed on the ACE monomer structure revealed 4 types of potential motion, termed bending, pivoting, breathing, and jumping (28). The breathing motion matches the open-close transition that dominates most of our principal component vectors, while the bending motion appears to correlate with the variance described by our top principal component vector. We did not observe any potential motions reminiscent of the jumping or pivoting motions in our 3DVA. Furthermore, the magnitude of the bending motion in our 3DVA is substantially less than previously reported for the partial dimeric

sACE structure, which likely suffered from substantial denaturation (28). Together, this highlights a significant difference in the conformational dynamics between sACE dimer and previously reported cryoEM structures. This type of analysis is sensitive to artifacts introduced by particle damage and denaturation, underscoring the importance of preserving protein integrity via sample preparation and the use of Chameleon to reduce the exposure to air-water interface. This also suggests dimerization functions as a key constraint to the conformational dynamics of sACE.

We then moved on to analyze our data using cryoDRGN, which revealed that the data formed a single cluster across multiple dimensions (Figure 5B, S10). Trajectories generated along five principal component vectors of structural variance were dominated by the open-close transition, primarily in sACE-N (Movie S8). We observed little variance in sACE-C and, unlike 3DVA, cryoDRGN did not reveal any substantial inter-domain motions. Faced with this discrepancy between the 3DVA and cryoDRGN results, we employed a third method, RECOVAR, to further analyze our data. Similar to cryoDRGN, RECOVAR revealed that our data formed a singular cluster across multiple dimensions of analysis. Volumes representative of kmeans cluster reconstructions were similarly consistent with our cryoDRGN results. RECOVAR indicated that the primary source of structural variance could be explained by the open-close transition, primarily of the sACE-N domains. With this in mind, we repeated the RECOVAR analysis with a focus mask around the sACE-N/N region. We then estimated the conformational density by deconvoluting the multidimensional latent space with a two-dimensional principal component analysis. The resulting density plot revealed four clusters which corresponded to different conformations of the sACE-N/N region (Figure 5C). The most populous cluster corresponded to a state where both sACE-N subunits adopted an open conformation. The second largest cluster, and the smallest cluster, corresponded to a state where one sACE-N was open and the other was closed. The discrepancy in population size between these clusters is likely due to bias in the initial particle poses, rather than a subunit-specific preference for the open state. The final cluster corresponded to a state where both sACE-N subunits adopted the closed conformation. We then used RECOVAR to generate a trajectory through the latent space to predict a potential transition pathway from the closed-closed state to the open-open state (Movie S9). This trajectory revealed that one subunit would open, followed by the second, and raised the question of potential allostery

355 or coordinated motion between the adjacent sACE-N domains. 3DVA, cryoDRGN, and
356 RECOVAR all appeared to display varying degrees of coordinated motion between sACE
357 domains, yet this type of analysis lacks an explicit time component, so it is not possible
358 to draw concrete conclusions regarding coordinated motion. Likewise, while MD
359 simulations contain an explicit time factor, most of our MD simulations closed quickly, and
360 did not reopen. Thus, while we did not observe coordinated motion from our simulations,
361 no conclusion can be reached because of limited intradomain motions. To investigate
362 coordination between the sACE-N domains, we performed 3D classification in
363 cryoSPARC with a focus mask on a single sACE-N domain and requested 2 classes
364 (Figure 5D). The particles were split roughly evenly between the two classes, one
365 resulting in an open state and the other being closed. We then used these classes for
366 another round of 3D classification with a focus mask on the opposite sACE-N domain and
367 again asked for 2 classes. Again, these particles were split roughly evenly among the
368 classes, leaving us with four similarly sized classes adopting the same conformations as
369 the clusters revealed by RECOVAR. As a result, we are unable to find any evidence of
370 coordinated motion between sACE-N domains in the absence of substrate.

371 **Discussion**

372 Our cryoEM and MD simulations analysis of the extracellular regions of dimeric
373 ACE offers insights into the stability of ACE catalytic domains. We show that ACE dimer
374 interface consists of three major components, protein-protein interfaces between ACE-N,
375 glycan-glycan interaction between ACE-N, and protein-protein interface between ACE-C.
376 The interface between ACE-N, in general, is 50% larger and has higher numbers of
377 hydrogen bonds and salt bridges than that between ACE-C. The necessity for the stronger
378 interaction between ACE-N is likely due to that ACE-N is distal to transmembrane helix
379 so that the additional reinforcement is required. The weaker interaction and lack in the
380 contribution from glycan in the interface between ACE-C could also explain the observed
381 preferential denaturation of ACE-C despite the high structural similarity between ACE-N
382 and ACE-C. The denaturation is likely due to the exposure to air-water interface during
383 vitrification, a common issue in single particle cryoEM analysis (35, 36). We have partially
384 overcome the denaturation issue of ACE-C by optimizing the buffer pH to increase the
385 melting temperature and using the faster plunging time during vitrification afforded by

386 Chameleon to reduce the exposure to air-water interface (Figure 1). However, we did not
387 completely prevent the preferential denature of ACE-C during vitrification.

388 ACE is part of a family of proteases capable of effectively degrading Aβ. This family
389 includes M16 metalloproteases like IDE and PreP, and M13 metalloproteases such as
390 neprilysin and endothelin converting enzyme. Integrative structural analysis has
391 demonstrated how IDE employs conformational dynamics, charge, and secondary
392 structure complementarity to selectively capture peptide substrates into its sizable
393 catalytic chamber, subsequently unfolding and degrading amyloidogenic peptides such
394 as insulin and Aβ, without degrading structurally similar yet non-amyloidogenic peptides
395 (25, 26, 52). The other mentioned enzymes also belong to this group of chamber-
396 containing proteases, known as cryptidases (24, 25, 53). Similar to cryptidases, structural
397 analysis reveals that ACE must undergo an open-closed transition to capture, engulf, and
398 degrade its oligopeptide substrates, such as angiotensin 1 and bradykinin.

399 Our apo-ACE structures and MD simulations identify a fulcrum mechanism that
400 governs the open-closed transition of ACE-N, while the interplay between ACE-N and the
401 D3a domain likely plays a crucial role in this transition. Analogous to the binding of MB60,
402 a PreP inhibitor, to the hydrophobic pocket to trigger the open to closed transition, factors
403 such as binding of substrates and ACE inhibitors may alter the balance, leading to the
404 regulation of ACE activity (24). We also observe that the catalytic pocket of the ACE
405 catalytic domain is not large enough to engulf the entire Aβ. Additionally, the distances
406 between the domains (ACE-N to ACE-C, ACE-N to ACE-N, or ACE-C to ACE-C) are too
407 large for these domains to bind Aβ simultaneously (54). Therefore, ACE likely employs a
408 different mechanism from IDE and PreP to selectively bind and degrade Aβ. Future
409 integrative structural studies await to reveal how ACE selectively recognizes and
410 degrades a diverse array of substrates.

411 Single particle cryoEM holds significant promise for revealing the conformational
412 dynamics of biological macromolecules from embedded heterogeneity. Consequently,
413 cryoEM heterogeneity analysis is an active and rapidly evolving field providing insights
414 into the conformational dynamics and allostery of macromolecules (47). However, many
415 challenges exist in using cryoEM heterogeneity analysis due, in part, to the low signal-to-
416 noise ratio in observed micrographs. Often, these analyses address questions difficult or
417 impossible to tackle experimentally, leaving no ground truth for validation. We encounter

418 such challenges in our heterogeneity analysis as well. Consistent with our single particle
419 cryoEM structural analysis, we observed the expected intradomain open-closed transition
420 using cryoDRGN, cryoSPARC 3DVA, RECOVAR, and all-atom MD simulation.
421 Surprisingly, we did not observe such motion using cryoSPARC 3DFlex, a neural network-
422 based method analyzing our cryoEM data of sACE (48). Central to the working of
423 cryoSPARC 3DFlex is the generation of a tetrahedral mesh used to calculate
424 deformations within the particle population. Proper generation of the mesh is critical for
425 obtaining useful results and must often be determined empirically. Despite several
426 attempts, we were unable to obtain mesh conditions suitable to observe any open-close
427 transition, illustrating a limitation of cryoSPARC 3DFlex.

428 The interplay between ACE-N and ACE-C within the ACE dimer has complicated
429 consequences for ACE functions, showing negative cooperativity for enzymatic activities
430 while exhibiting positive synergy in Aβ cleavage by ACE-N and activity at the bradykinin
431 receptor (11, 31-34). Understanding the conformational dynamics in both inter- and intra-
432 domain motions of the extracellular regions of the ACE dimer holds promise for designing
433 ACE modulators to improve and broaden the therapeutic use of ACE modulation. Our
434 cryoEM heterogeneity analysis has revealed coordinated open-closed transitions across
435 four catalytic domains using cryoDRGN and cryoSPARC 3DVA, which could potentially
436 provide the molecular basis for ACE allostery (Figure 5A,B, Movies S7,8). However, our
437 RECOVAR analysis reveals independent motion of two ACE-N domains, not the
438 coordinated motion revealed by cryoDRGN and cryoSPARC 3DVA (Figure 5C).
439 Furthermore, our focused classification using cryoSPARC failed to reveal a profound
440 association between specific conformational states of the ACE catalytic domains, an
441 expectation from the trajectories revealed by cryoDRGN and cryoSPARC 3DVA (Figure
442 5D).

443 The first principal component trajectory in our 3DVA analysis revealed a significant
444 potential interdomain motion between sACE-N/N and sACE-C/C, yet cryoDRGN and
445 RECOVAR did not reveal any inferred motions of similar magnitude. Notably, the
446 trajectory revealing this potential interdomain motion in 3DVA was absent any variability
447 in the sACE-N open/close transition. In our study, this conformational heterogeneity
448 appears to stem from subtle yet significant conformational differences between the two
449 chains within an ACE dimer and the inability of cryoSPARC to properly align these

450 conformationally distinct chains (Figure S11). CryoDRGN and RECOVAR revealed
451 smaller magnitudes of potential interdomain motions, which were often accompanied by
452 various combinations of individual domains opening and/or closing. This suggests that
453 the apparent discrepancy in the magnitude of inferred interdomain motion could be a
454 result of the different theoretical approaches of dimensionality reduction and trajectory
455 generation employed by the respective methods of analysis and underscores the
456 importance of incorporating multiple methods of analysis in the absence of a singular
457 "gold-standard" of heterogeneity analysis.

458 Advances in single-particle cryoEM analysis have enabled detailed structural
459 examination of the extracellular domains of the ACE dimer. Beyond its implications for
460 future drug discovery efforts aimed at enhancing ACE-based therapies, ACE can serve
461 as a valuable model of a multi-domain glycoprotein for studying methods to preserve
462 sample integrity, particularly due to the high propensity of ACE-C to denature during
463 vitrification. Furthermore, considering the aforementioned challenges and caveats, we
464 propose that, due to its size, biomedical importance, and the complexity of its motions,
465 ACE also represents an excellent model system for evaluating and improving cryoEM
466 heterogeneity analysis.

467 **Experimental procedures**

468 **Expression of human sACE**: Human 293T and 293F cells were maintained in DMEM +
469 10% fetal calf serum (FCS). The lentiviral plasmid for the expression of the extracellular
470 domain of human ACE (sACE, aa 1-1231) that contains a 6-histidine tag at its C-terminus
471 was made by Vectorbuilder and co-transfected with helper plasmids to human 293T cells
472 for lentiviral production. Human 293F cells were infected with the resulting virus and
473 selected for stable sACE expression. 293F that stably expressed sACE grew poorly in
474 Free-style 293 media (ThermoFisher 12338018). Thus, for ACE production, 293F cells
475 that stably expressed sACE were first grown in DMEM+10% FCS at 37°C and gradually
476 shifted into Free-style 293 media by reducing FCS by first in Free-style 293 media + 2%
477 FCS and then to media without FCS. These cells were then shifted to and maintained in
478 30°C for 3-5 days for ACE production to reduce proteolysis.

479 **Purification of soluble human ACE:** Culture supernatant was centrifuged at 3,000xg for
480 5 min, diluted 10-fold with 25 mM Tris-HCl pH 8, filtered, and run over a Source Q column

481 pre-equilibrated with 25 mM Tris-HCl pH 8. Column was washed to baseline with Tris-HCl
482 pH 8 and bound protein was eluted with a linear gradient of NaCl to 1 M. sACE containing
483 fractions were pooled and EDTA was added to 10 mM to strip the catalytic zinc ion.
484 Sample was concentrated and run over a Superdex S200 SEC column pre-equilibrated
485 with the desired cryoEM buffer.

486 **Differential scanning fluorometry (DSF)**: To optimize the grid making conditions,
487 differential scanning fluorimetry was applied to screen 96 buffers conditions. DSF was
488 performed with 3 mg/ml sACE and 10X Sypro Orange in 20 µl buffers in a Thermo Fisher
489 Step ONE RT-PCR thermocycler. Using the melting temperature and slope as selective
490 criteria, 25 mM citrate pH 5.5, 25 mM sodium phosphate pH 5.5, 150 mM NaCl, 10 mM
491 EDTA was identified as the ideal buffer condition and used for all subsequent cryoEM
492 experiments.

493 **CryoEM data collection and processing:** Peak fractions were collected off the SEC
494 column and used to immediately prepare grids, resulting in a protein concentration of ~4.5
495 mg/ml. Quantifoil R1.2/1.3 Cu200 grids were glow-discharged in air and grids were
496 prepared by Vitrobot mark 3. 3.5 µl of sample was applied to the grid in the chamber with
497 100% humidity, 25°C. Excess sample was blotted for 1 sec, blot force 2, and grids were
498 plunge frozen in liquid ethane. All images were acquired using a Titan Krios microscope
499 (FEI) operated at 300KeV with a Gatan K3 direct electron detector. A dataset of ~3,600
500 micrographs was collected at The University of Chicago Advanced Electron Microscopy
501 facility. The dataset was processed using cryoSPARC (Figure S1) (55). Briefly, a four-
502 domain sACE dimer model was generated using sACE-N dimer and sACE monomer and
503 adjusting the distance between ACE-C domains to avoid steric clashes as a template for
504 particle picking (28). After template picking, 1.1 million particles were extracted with a box
505 size of 360 pixels. Several rounds of 2D classification were used to remove junk particles.
506 ~577K particles were processed in successive rounds of *ab initio* reconstruction and
507 heterogeneous refinement. sACE grids were also prepared using Chameleon and
508 collected a dataset of ~19,000 micrographs at the National Center for CryoEM Access
509 and Training. For those, Quantifoil Active R 1.6/0.9 Cu/Rh 300 were coated with gold
510 using a Safematic CCU-010 Compact Coating Unit. Briefly, grids were placed nanowire
511 side down on a glass slide, gold disks were sputtered with a 35 nm target thickness at 1.5
512 x 10^{-2} Torr, and a process current of 30 mA. Grids were glow discharged with air at 12mA

513 for 80 secs using the internal Chameleon glow discharger. The grids were plunged at 160
514 to 180 milliseconds. All images were acquired using a Titan Krios microscope (FEI)
515 operated at 300KeV with a Gatan K3 direct electron detector (Gatan). Images were
516 automatically acquired using Leginon (56) using collection parameters as shown in Table
517 S1. This dataset was processed in cryoSPARC (Figure S2). Briefly, templates were
518 generated from our full-length ACE structure described above using vitrobot-prepared
519 grids. Micrographs with a max CTF value worse than 4Å were removed from the dataset,
520 leaving ~12,000 micrographs for template picking, which yielded 10.7 million particles.
521 The particle set was trimmed to ~2.8 million based on quality metrics and run through 2
522 rounds of 2D classification, reducing the particle number to ~660,000. 2D classes were
523 dominated by 4 domain views, and yielded a much greater diversity of views, indicating
524 that Chameleon preparation produced a dramatic improvement in particle quality. Initial
525 3D homogeneous refinement reached 3.6 Å, matching the previous final structure. Four
526 maps from 3D classes that contains all four catalytic domains of ACE, one from particles
527 derived from grids prepared by using vitrobot and three from those prepared by using
528 Chameleon, were used for structure building using Chimera and Coot and the structure
529 was refined using Phenix real space refinement. Structural analysis was performed using
530 PYMOL and Chimera.

531 **Heterogeneity analysis**: All heterogeneity analysis was performed on the full final
532 particle set, encompassing all of the NCCAT structures. Initially, cryoSPARC 3DVA was
533 performed on both the NCCAT- and UChicago-collected datasets and results were found
534 to be consistent, so the NCCAT-collected dataset was used for further analysis, given its
535 higher particle number and quality. Input particle poses for each method of heterogeneity
536 analysis were derived from the same C1 refinement job in cryoSPARC, which reached
537 2.88 Å. 3DVA was used to solve the top 5 modes of variance with a filter resolution of 6
538 Å. Particles were downsampled ~3x to a box size of 128 pixels in cryoDRGN to speed up
539 processing. The same downsampled particle set was used for both cryoDRGN and
540 RECOVAR. CryoDRGN was run with default parameters and the analysis was performed
541 on the top 5 principal components for direct comparison to cryoSPARC 3DVA. RECOVAR
542 pipeline.py was initially run on the full sACE structure. Reconstructions representative of
543 kmeans cluster centers revealed the dominant source of structural variability to be the
544 open-close transition in sACE-N. As a result, RECOVAR was run again with a focus mask

545 on sACE-N/N and a zdim=4. Conformational density was estimated with a 2-dimensional
546 PCA, and an index value of 3 was chosen for further analysis. The points in latent space
547 representing the top 12 stable conformational states were estimated from the top 20% of
548 particles and representative volumes were generated. The generated states populated
549 four clusters and the 12 states were simplified to 4 distinct conformations where sACE-
550 N/N adopted the open-open (OO), open-closed (OC), closed-open (CO), and closed-
551 closed (CC) states (Figure 5C). We then generated a trajectory through the latent space
552 using the OO and CC representative volumes as endpoints (Movie S7).

553 **All-atom MD simulations and analysis**: The sACE-3.65 structure was used to initiate
554 all MD simulations. For the glycosylated sACE simulations, N-linked glycans were built
555 onto all 12 known N-linked glycosylation sites (residues 38, 54, 74, 111, 146, 318, 445,
556 509, 677, 695, 714, 760) with the complex glycan BGLC-BGLC-BMAN-AMAN-BGLC-
557 ANE5-AMAN-BGLC-BGAL-ANE5-AFUC using CHARMM-GUI (57). Simulations were
558 prepared in QwikMD or CHARMM-GUI and run at pH 7, 150 mM NaCl, 310 K, 1 atm with
559 periodic boundary conditions in NAMD3.0 using the University of Chicago Beagle3
560 partition (58). Explicit solvent was described with the TIP3P model (59). Data was
561 analyzed in VMD 1.9.4 (60).

Figure + figure legends:

Figure 1: CryoEM analysis of human ACE dimer. (A) Diagram for the key features of domain on primary sequence of human ACE. To avoid confusion existing in the numbering of ACE structures, we number ACE based on Uniprot P12821-1. D1a and D3a domains, also called "lid" encompasses residues 31-127 and aa 645-725, respectively. D1b and D3b domains each have two discrete segments; residues 292-465 and 525-603 for D1b and residues 897-1060 and 1120-1200 for D3b. D2 encompasses three discrete segments, residues 128-291, 466-524, and 604-644 while D4 domain encompasses residues 726-896, 1061-1119, and 1201-1231. sp = signal peptide. asterisk = zinc binding motif. The construct used in this study comprises residues 1-1231, which we refer to as the soluble region of ACE (sACE). Colored by sub-domain: D1a cyan, D1b aqua, D2 pink, D3a light blue, D3b green, D4 magenta. (B) 2D classification of human sACE particles from grids made by vitrobot and Chameleon. Clear four domain classes visible in the Chameleon-derived classification are boxed in red, similar views are lacking in the vitrobot dataset. (C) Full-length sACE 3D volumes, colored by sub-domain as in (A). Glycan density is shown in gray. See Figure S2 for vitrobot-prepared data processing details, Figure S3 for Chameleon-prepared data processing details and Table S1 for data refinement statistics.

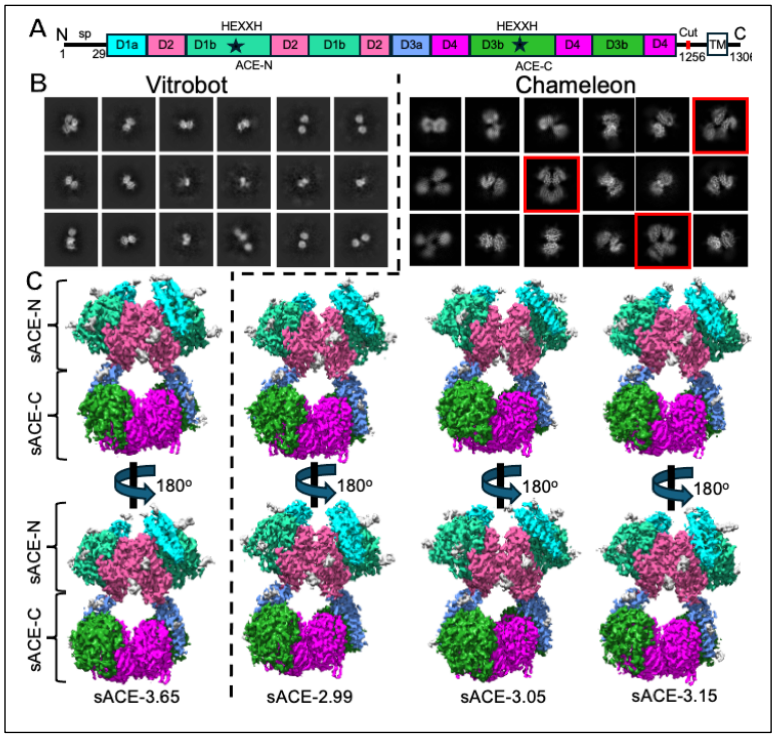

Figure 2: Overall structure of human ACE. (A) Overlay comparing sACE-N states highlighting the structure differences between the closed (C), intermediate (I), and open (O) states. (B) Overlay comparing sACE-C states highlighting the structure differences between the closed (C), and intermediate (I) states. We define the state based on the distance between the edge of the D2/4 domain bordering the catalytic cleft (residues 150-155 or 750-755) and the tip of the D1/3a region (residues 70-80 or 676-686): closed <15 Å, intermediate >15 Å and <19 Å, open >19 Å. (C) Overall dimer comparisons. (D) Table of openness measurements for each domain per structure.

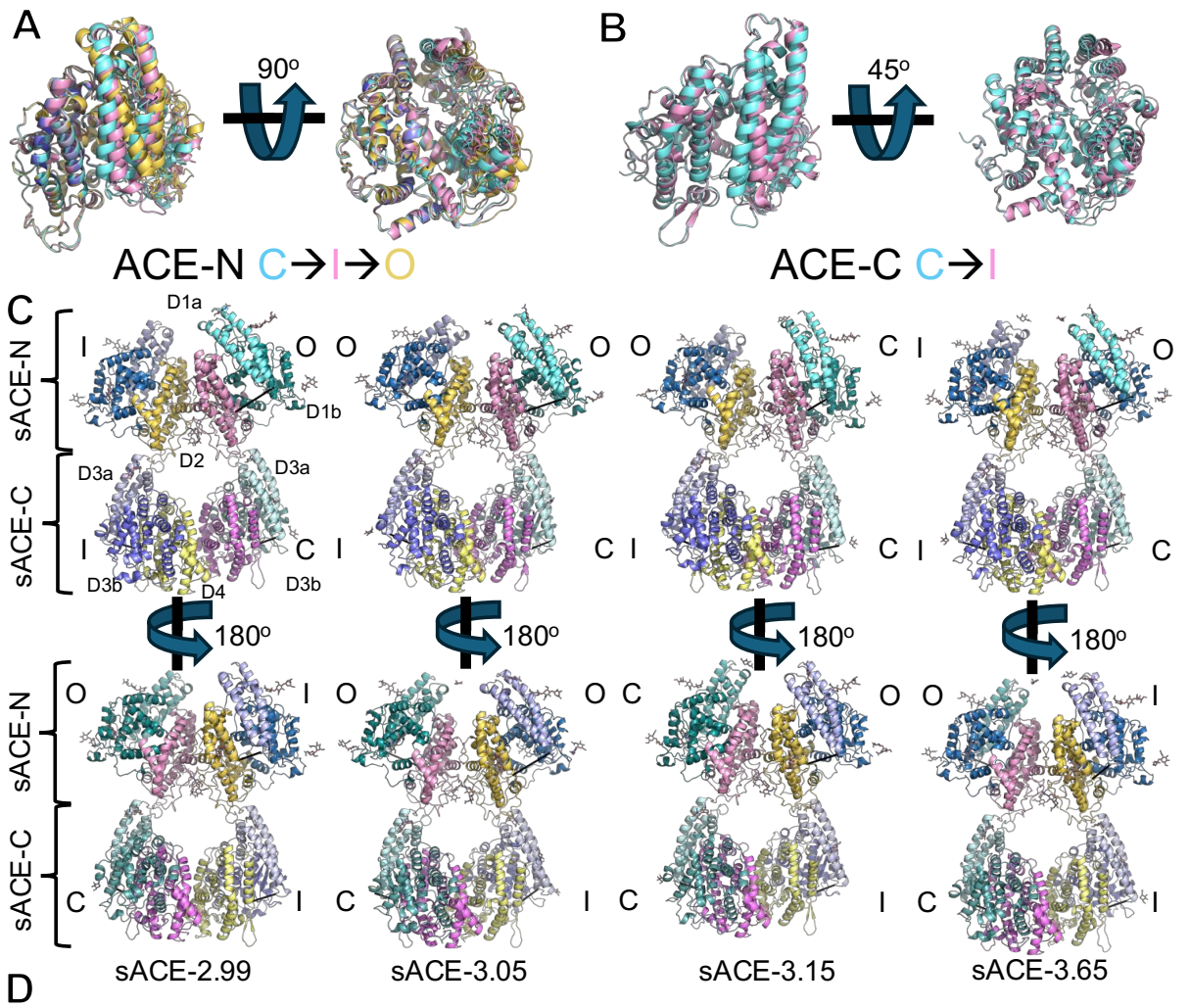

D

Opening distance (Å)	sACE-2.99		sACE-3.05		sACE-3.15		sACE-3.65	
	Chain A	Chain B	Chain A	Chain B	Chain A	Chain B	Chain A	Chain B
ACE-N	23.4 (O)	17.7 (I)	22.5 (O)	22.1 (O)	14.1 (C)	20.2 (O)	20.6 (O)	16.2 (I)
ACE-C	14.4 (C)	18.0 (I)	17.9 (I)	13.9 (C)	13.7 (C)	17.0 (I)	14.4 (C)	15.9(I)

590 Figure 3: sACE dimerization interfaces. (A) Overlay comparing sACE-N/N interface (blue)
591 and sACE-C/C (yellow) interfaces. Interfaces adopt the same secondary structure but
592 interacting residues vary between them. (B) Residue-specific interactions at the sACE-
593 N/N interface, see text for details. (C) Unsharpened Coulomb potential density map (cyan)
594 showing density corresponding to glycan-glycan interaction from N111 as part of sACE-
595 N/N interface. Sharpened map is shown in magenta for reference. (D) Residue-specific
596 interactions in the sACE-C/C interface, see text for details.

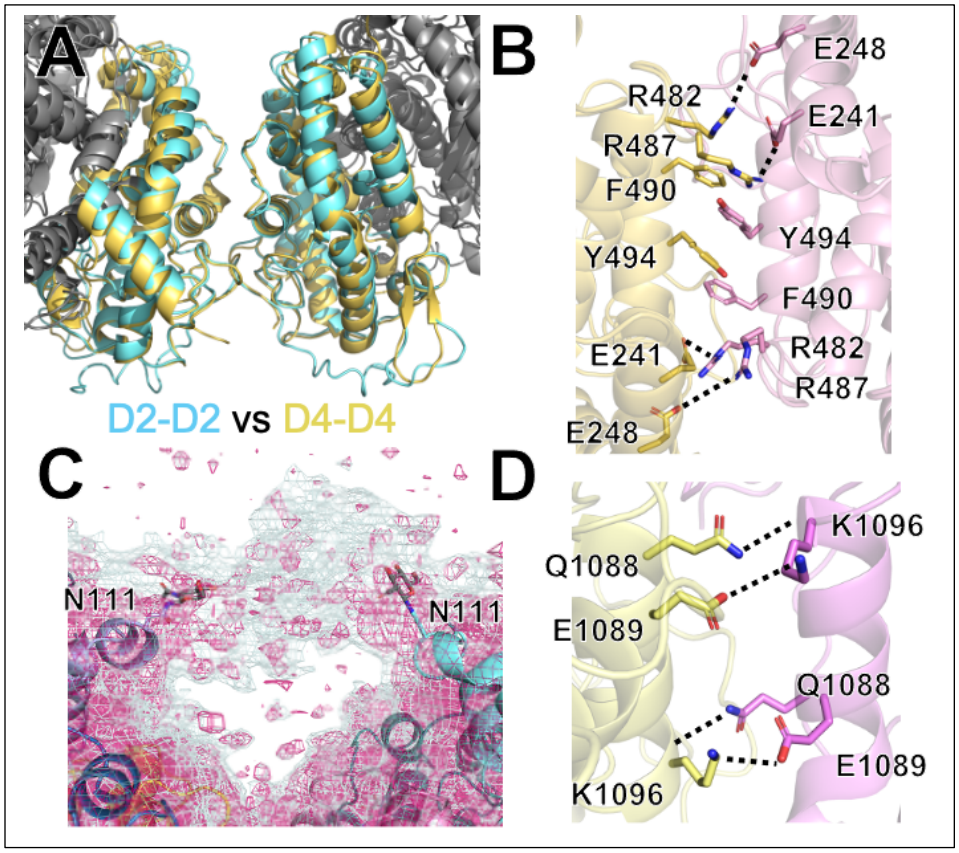

597

598 Figure 4: Structural mechanism of the sACE open/close transition. (A) sACE-N overlay
599 comparing the open (colored in left panel, transparent gray in right panel) and closed
600 (transparent gray in left panel, colored in right panel) states in detail. The open state is
601 stabilized by interaction between residues in the D1a (cyan) and D2 (pink) regions that,
602 notably K102-D218. In the closed state, the K102-D218 interaction is broken. (B) Overlay
603 of the sACE-N open (cyan) and closed (pink) states showing the range of motion. The
604 D1a region rotates about a fulcrum region described in (A), while the D1b region moves
605 as a rigid body. (C) Overlay of sACE-C closed (light blue) and intermediate (yellow) states.
606 Unlike sACE-N, the “top” of the D3a region is constrained by its connection to sACE-N

607 and largely immobile. The primary source of opening is only the motion of the D3a tip. We
608 did not observe any open state structures of sACE-C, suggesting a smaller range of
609 motion relative to sACE-N. (D) Comparison of the hydrophobic “latch” region formed in
610 the closed state between residues of the D1/3a, D1/3b, and D2/D4 domains. V753 in
611 sACE-C has been replaced by T153 in sACE-N, suggesting that the closed state in sACE-
612 N may be less stabilized than the sACE-C closed state. (E) Example all-atom MD
613 simulation tracking the openness of one sACE-N region (black line) and this distance
614 between K102 and D218 (red line). These residues form a salt bridge early in the
615 simulation when sACE-N is open (left inset) but the interaction breaks as sACE-N
616 transitions to the closed state (right inset). Distance measurements for MD simulations
617 were consistently greater than distance values in our static structures and cannot be
618 directly compared to Figure 2.

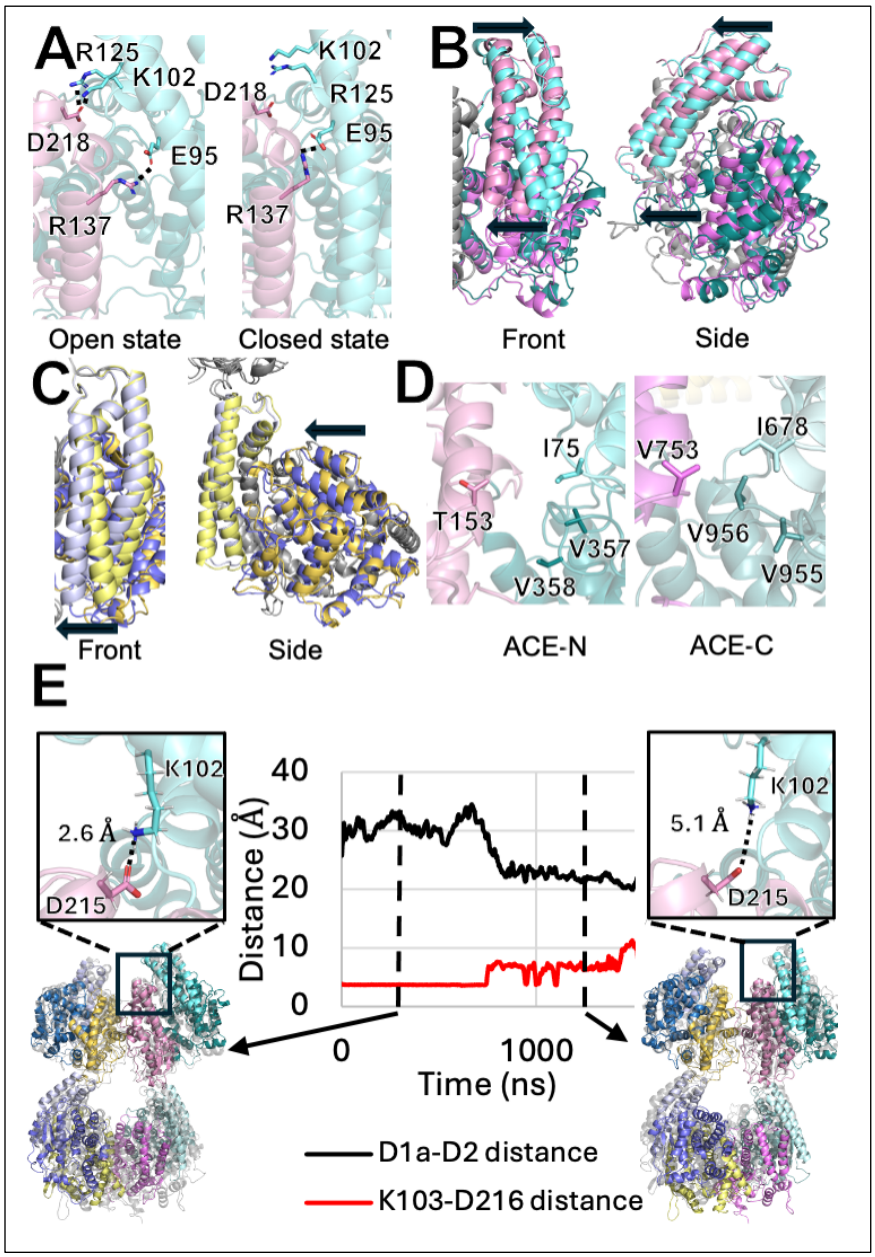

Figure 5: CryoEM heterogeneity analysis. (A) Visualization of the structural changes revealed by cryoSPARC 3DVA trajectories calculated along two principal components (PCs) of structural variance. Starting states are showing in cyan, ending states in gray. PC 0 reveals a large, inter-domain bending motion accompanied by the open/close transition in sACE-C. PC 1 and the remaining PCs are dominated by the open/close transition of individual regions. See Table S3, and Movie S7 for additional details. (B) Visualization of the structural changes revealed by the cryoDRGN trajectories calculated along two PCs of structural variance. Starting states are shown in cyan, ending states in gray. PCs are dominated by the open/close transition of individual regions. See Table S3, and Movie S8 for additional details. (C) Analysis in RECOVAR with a focus mask on

sACE-N/N reveals that particles adopt roughly four clusters within the latent space (heat map of particle density) corresponding to the open-open (OO, white square), open-closed (OC, white dot), closed-open (CO, white dot) and closed-closed (CC, white star) states of sACE-N/N. A trajectory estimating the path through latent space corresponding to the structural transition from sACE-N/N CC state to the OO state (blue points) suggests that individual sACE regions transition at different rates. See Movie S9 for trajectory. (D) Focused 3D classification was performed in cryoSPARC to explore evidence of coordinated motion between sACE-N regions. 3D classification focusing on one sACE-N region revealed 2 roughly equal classes of particles: open and closed. Subsequent 3D classification focused on the other sACE-N region again revealed 2 roughly equal classes, suggesting the lack of coordinated motion between sACE-N regions in the absence of substrate.

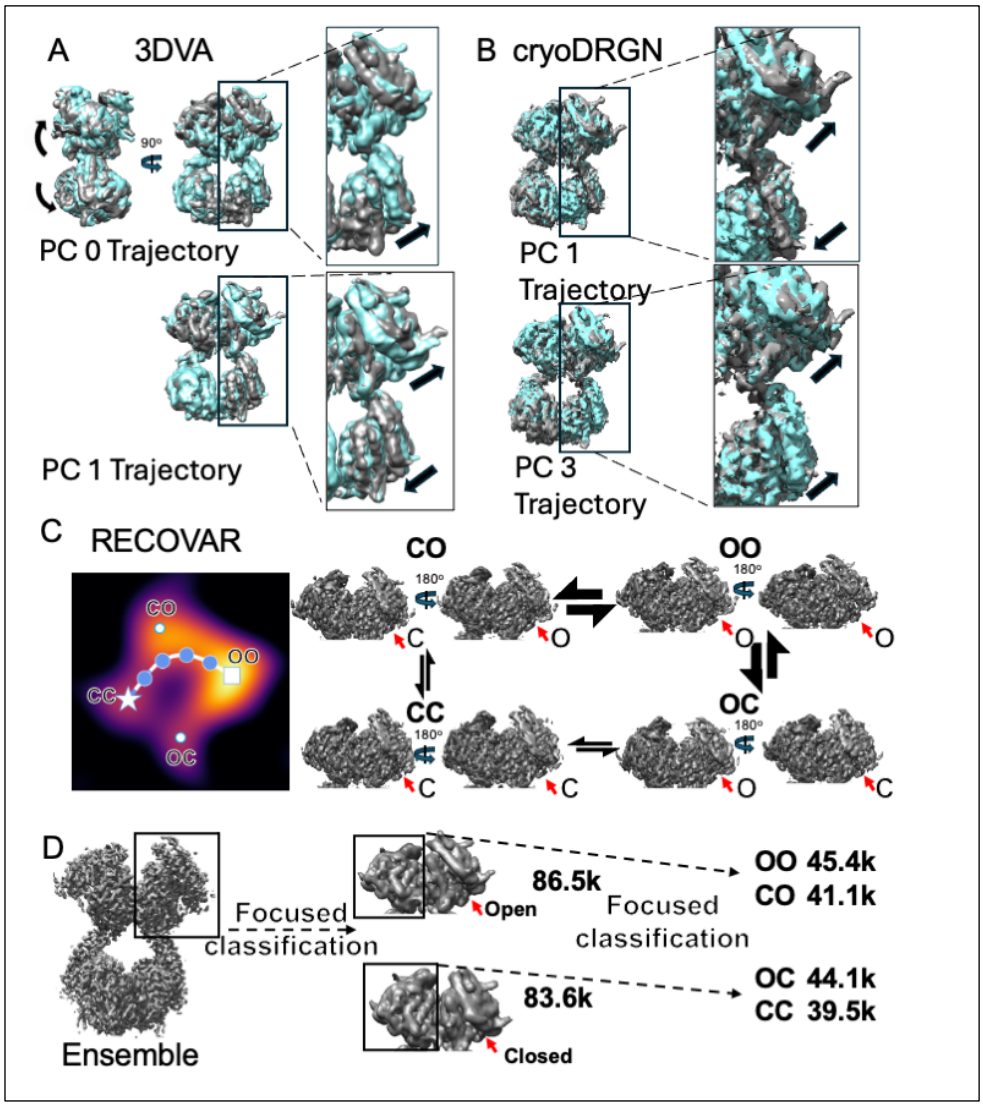

Data availability:

Unprocessed micrographs, particle stacks, and associated pose/CTF information have been deposited to EMPIAR under the accession numbers: EMPIAR-12181 (Vitrobot-prepared grids) and EMPIAR-12484 (Chameleon-prepared grids)

EM structures and maps have been deposited to the EMDB and PDB, respectively, under the following accession numbers:

sACE-2.99: 9D5S and EMD-46581

sACE-3.05: 9D5M and EMD-46579

sACE-3.15: 9D55 and EMD-46574

sACE-3.65: 9CLX and EMD-45733

References:

1. K. E. Bernstein *et al.*, A Modern Understanding of the Traditional and Nontraditional Biological Functions of Angiotensin-Converting Enzyme. *Pharmacol Rev* **65**, 1-46 (2013).
2. L. Lubbe, G. E. Cozier, D. Oosthuizen, K. R. Acharya, E. D. Sturrock, ACE2 and ACE: structure-based insights into mechanism, regulation and receptor recognition by SARS-CoV. *Clin Sci* **134**, 2851-2871 (2020).
3. A. J. Turner, N. M. Hooper, The angiotensin-converting enzyme gene family: genomics and pharmacology. *Trends Pharmacol Sci* **23**, 177-183 (2002).
4. L. L. Herman, S. A. Padala, I. Ahmed, K. Bashir, "Angiotensin-Converting Enzyme Inhibitors (ACEI)" in StatPearls. (Treasure Island (FL) ineligible companies. Disclosure: Sandeep Padala declares no relevant financial relationships with ineligible companies. Disclosure: Intisar Ahmed declares no relevant financial relationships with ineligible companies. Disclosure: Khalid Bashir declares no relevant financial relationships with ineligible companies., 2024).
5. M. Semis, G. B. Gugiu, E. A. Bernstein, K. E. Bernstein, M. Kalkum, The Plethora of Angiotensin-Converting Enzyme-Processed Peptides in Mouse Plasma. *Anal Chem* **91**, 6440-6453 (2019).
6. W. Y. Zheng *et al.*, Small molecule angiotensin converting enzyme inhibitors: A medicinal chemistry perspective. *Front Pharmacol* **13** (2022).
7. K. E. Bernstein *et al.*, Angiotensin-converting enzyme in innate and adaptive immunity. *Nat Rev Nephrol* **14**, 325-336 (2018).
8. R. Danziger *et al.*, The effects of enhancing angiotensin converting enzyme in myelomonocytes on ameliorating Alzheimer's-related disease and preserving cognition. *Front Physiol* **14**, 1179315 (2023).
9. H. Hampel *et al.*, The Amyloid-β Pathway in Alzheimer's Disease. *Mol Psychiatr* **26**, 5481-5503 (2021).
10. M. L. Hemming, D. J. Selkoe, Amyloid beta-protein is degraded by cellular angiotensin-converting enzyme (ACE) and elevated by an ACE inhibitor. *J Biol Chem* **280**, 37644-37650 (2005).
11. K. Zou *et al.*, A beta 42-to-A beta 40-and Angiotensin-converting Activities in Different Domains of Angiotensin-converting Enzyme. *J Biol Chem* **284**, 31914-31920 (2009).
12. Y. Zhang, H. Chen, R. Li, K. Sterling, W. Song, Amyloid beta-based therapy for Alzheimer's disease: challenges, successes and future. *Signal Transduct Target Ther* **8**, 248 (2023).
13. K. E. Bernstein *et al.*, Angiotensin-converting enzyme overexpression in myelomonocytes prevents Alzheimer's-like cognitive decline. *J Clin Invest* **124**, 1000-1012 (2014).
14. F. Gouveia *et al.*, Targeting brain Renin-Angiotensin System for the prevention and treatment of Alzheimer's disease: Past, present and future. *Ageing Res Rev* **77** (2022).
15. J. W. Wright, L. H. Kawas, J. W. Harding, A Role for the Brain RAS in Alzheimer's and Parkinson's Diseases. *Front Endocrinol (Lausanne)* **4**, 158 (2013).
16. W. Q. Qiu *et al.*, Angiotensin Converting Enzyme Inhibitors and the Reduced Risk of Alzheimer's Disease in the Absence of Apolipoprotein E4 Allele. *J Alzheimers Dis* **37**, 421-428 (2013).
17. J. F. Riordan, Angiotensin-I-converting enzyme and its relatives. *Genome Biol* **4**, 225 (2003).
18. W. R. English, P. Corvol, G. Murphy, LPS activates ADAM9 dependent shedding of ACE from endothelial cells. *Biochem Bioph Res Co* **421**, 70-75 (2012).
19. F. X. Gomis-Ruth, Structure and Mechanism of Metallocarboxypeptidases. *Critical Reviews in Biochemistry and Molecular Biology* **43**, 319-345 (2008).
20. K. R. Acharya, K. S. Gregory, E. D. Sturrock, Advances in the structural basis for angiotensin-1 converting enzyme (ACE) inhibitors. *Bioscience Rep* **44** (2024).

21. H. R. Corradi, S. L. Schwager, A. T. Nchinda, E. D. Sturrock, K. R. Acharya, Crystal structure of the N domain of human somatic angiotensin I-converting enzyme provides a structural basis for domain-specific inhibitor design. *J Mol Biol* **357**, 964-974 (2006).
22. G. Masuyer, S. L. U. Schwager, E. D. Sturrock, R. E. Isaac, K. R. Acharya, Molecular recognition and regulation of human angiotensin-I converting enzyme (ACE) activity by natural inhibitory peptides. *Sci Rep* **2**, 717 (2012).
23. R. Natesh, S. L. Schwager, E. D. Sturrock, K. R. Acharya, Crystal structure of the human angiotensin-converting enzyme-lisinopril complex. *Nature* **421**, 551-554 (2003).
24. W. G. Liang *et al.*, Structural basis for the mechanisms of human presequence protease conformational switch and substrate recognition. *Nat Commun* **13**, 1833 (2022).
25. E. Malito, R. E. Hulse, W. J. Tang, Amyloid β-degrading cryptidases: insulin degrading enzyme, presequence peptidase, and neprilysin. *Cell Mol. Life Sci.* **65**, 2574-2585 (2008).
26. Z. N. Zhang *et al.*, Ensemble cryoEM elucidates the mechanism of insulin capture and degradation by human insulin degrading enzyme. *Elife* **7**, e33572 (2018).
27. G. E. Cozier, L. Lubbe, E. D. Sturrock, K. R. Acharya, Angiotensin-converting enzyme open for business: structural insights into the subdomain dynamics. *FEBS J* **288**, 2238-2256 (2021).
28. L. Lubbe, B. T. Sewell, J. D. Woodward, E. D. Sturrock, Cryo-EM reveals mechanisms of angiotensin I-converting enzyme allostery and dimerization. *EMBO J* **41**, e110550 (2022).
29. T. T. V. Phan, S. Y. Heo, W. K. Jung, M. Yi, Spontaneous Hinge-Bending Motions of Angiotensin I Converting Enzyme: Role in Activation and Inhibition. *Molecules* **25**, 1288 (2020).
30. K. E. Bernstein *et al.*, Different in vivo functions of the two catalytic domains of angiotensin-converting enzyme (ACE). *Curr Opin Pharmacol* **11**, 105-111 (2011).
31. P. V. Binevski, E. A. Sizova, V. F. Pozdnev, O. A. Kost, Evidence for the negative cooperativity of the two active sites within bovine somatic angiotensin-converting enzyme. *Febs Lett* **550**, 84-88 (2003).
32. G. I. Rice, D. A. Thomas, P. J. Grant, A. J. Turner, N. M. Hooper, Evaluation of angiotensin-converting enzyme (ACE), its homologue ACE2 and neprilysin in angiotensin peptide metabolism. *Biochem J* **383**, 45-51 (2004).
33. O. E. Skirgello, P. V. Binevski, V. F. Pozdnev, O. A. Kost, Kinetic probes for inter-domain co-operation in human somatic angiotensin-converting enzyme. *Biochem J* **391**, 641-647 (2005).
34. E. G. Erdos, F. Tan, R. A. Skidgel, Angiotensin I-converting enzyme inhibitors are allosteric enhancers of kinin B1 and B2 receptor function. *Hypertension* **55**, 214-220 (2010).
35. R. M. Glaeser, Proteins, interfaces, and cryo-EM grids. *Curr Opin Colloid In* **34**, 1-8 (2018).
36. A. J. Noble *et al.*, Reducing effects of particle adsorption to the air-water interface in cryo-EM. *Nat Methods* **15**, 793-795 (2018).
37. S. Voronov, N. Zueva, V. Orlov, A. Arutyunyan, O. Kost, Temperature-induced selective death of the C-domain within angiotensin-converting enzyme molecule. *Febs Lett* **522**, 77-82 (2002).
38. M. C. Darrow, J. P. Moore, R. J. Walker, K. Doering, R. S. King, Chameleon: Next Generation Sample Preparation for CryoEM based on Spotiton. *Microscopy and Microanalysis* **25**, 994-995 (2019).
39. H. R. Corradi, S. L. U. Schwager, A. T. Nchinda, E. D. Sturrock, K. R. Acharya, Crystal structure of the N domain of human somatic angiotensin I-converting enzyme provides a structural basis for domain-specific inhibitor design. *Journal of Molecular Biology* **357**, 964-974 (2006).
40. R. Natesh, S. L. U. Schwager, E. D. Sturrock, K. R. Acharya, Crystal structure of the human angiotensin-converting enzyme-lisinopril complex. *Nature* **421**, 551-554 (2003).
41. O. A. Kost, N. V. Bovin, E. E. Chemodanova, V. V. Nasonov, T. A. Orth, New feature of angiotensin-converting enzyme: carbohydrate-recognizing domain. *J Mol Recognit* **13**, 360-369 (2000).

42. H. G. O'Neill, P. Redelinghuys, S. L. U. Schwager, E. D. Sturrock, The role of glycosylation and domain interactions in the thermal stability of human angiotensin-converting enzyme. *Biol Chem* **389**, 1153-1161 (2008).
43. R. Sadhukhan, I. Sen, Different glycosylation requirements for the synthesis of enzymatically active angiotensin-converting enzyme in mammalian cells and yeast. *J Biol Chem* **271**, 6429-6434 (1996).
44. B. Baudin, N. Alves, A. Pilon, B. Beneteau-Burnat, J. Giboudeau, Structural and biological roles of glycosylations in pulmonary angiotensin I-converting enzyme. *Glycobiology* **7**, 565-570 (1997).
45. T. Orth, S. Voronov, P. Binevski, W. Saenger, O. Kost, Glycosylation of bovine pulmonary angiotensin-converting enzyme modulates its catalytic properties. *Febs Lett* **431**, 255-258 (1998).
46. X. C. Yu *et al.*, Identification of N-linked glycosylation sites in human testis angiotensin-converting enzyme and expression of an active deglycosylated form. *J Biol Chem* **272**, 3511-3519 (1997).
47. W. S. Tang, E. D. Zhong, S. M. Hanson, E. H. Thiede, P. Cossio, Conformational heterogeneity and probability distributions from single-particle cryo-electron microscopy. *Curr Opin Struc Biol* **81** (2023).
48. A. Punjani, D. J. Fleet, 3DFlex: determining structure and motion of flexible proteins from cryo-EM. *Nature Methods* **20**, 860-+ (2023).
49. M. A. Gilles, A. Singer, Cryo-EM Heterogeneity Analysis using Regularized Covariance Estimation and Kernel Regression. *bioRxiv* 10.1101/2023.10.28.564422 (2024).
50. E. D. Zhong, T. Bepler, B. Berger, J. H. Davis, CryoDRGN: reconstruction of heterogeneous cryo-EM structures using neural networks. *Nature Methods* **18**, 176-+ (2021).
51. A. Punjani, D. J. Fleet, 3D variability analysis: Resolving continuous flexibility and discrete heterogeneity from single particle cryo-EM. *J Struct Biol* **213** (2021).
52. W. J. Tang, Targeting Insulin-Degrading Enzyme to Treat Type 2 Diabetes Mellitus. *Trends Endocrinol Metab* **27**, 24-34 (2016).
53. W. G. Liang, J. M. Mancl, M. Zhao, W. J. Tang, Structural analysis of Mycobacterium tuberculosis M13 metalloprotease Zmp1 open states. *Structure* **29**, 709-720 (2021).
54. G. F. Chen *et al.*, Amyloid beta: structure, biology and structure-based therapeutic development. *Acta Pharmacol Sin* **38**, 1205-1235 (2017).
55. A. Punjani, J. L. Rubinstein, D. J. Fleet, M. A. Brubaker, cryoSPARC: algorithms for rapid unsupervised cryo-EM structure determination. *Nat Methods* **14**, 290-296 (2017).
56. C. Suloway *et al.*, Automated molecular microscopy: The new Leginon system. *J Struct Biol* **151**, 41-60 (2005).
57. J. Lee *et al.*, CHARMM-GUI Input Generator for NAMD, GROMACS, AMBER, OpenMM, and CHARMM/OpenMM Simulations Using the CHARMM36 Additive Force Field. *J Chem Theory Comput* **12**, 405-413 (2016).
58. J. C. Phillips *et al.*, Scalable molecular dynamics on CPU and GPU architectures with NAMD. *J Chem Phys* **153** (2020).
59. W. L. Jorgensen, J. Chandrasekhar, J. D. Madura, R. W. Impey, M. L. Klein, Comparison of Simple Potential Functions for Simulating Liquid Water. *J Chem Phys* **79**, 926-935 (1983).
60. W. Humphrey, A. Dalke, K. Schulten, VMD: visual molecular dynamics. *J Mol Graph* **14**, 33-38, 27-38 (1996).